Peeping inside tropical cyclones with the WIVERN space-borne Doppler radar

Alessandro Battaglia[1,2], Massimiliano Recupero[1], Francesco Manconi[1], Cinzia Cambiotti[1], Marco Coppola[1], Antonio Parodi[3], Frederic Tridon[1], Simone Mantovani[4], Pavlos Kollias[5,6], Marcel Kleinherenbrink[7], Maryam Pourshamsi[7]

[1]Dipartimento di Ingegneria dell'Ambiente, del Territorio, Politecnico di Torino, Turin, Italy
[2]Department of Physics and Astronomy, University of Leicester, Leicester, United Kingdom
[3]CIMA Foundation, Savona, Italy
[4]MEEO, Ferrara, Italy
[5]School of Marine and Atmospheric Sciences, Stony Brook University, NY, USA
[6]Department of Atmospheric and Oceanic Sciences, McGill University, Montreal, QC, Canada
[7]European Space Agency, Noordwijk, The Netherlands

Key Points:

- The WIVERN mission concept aims to provide three-dimensional profiles of in-cloud winds and cloud structure across scales from 1 to 1000 km using its unique Doppler radar capabilities.
- WIVERN can provide three-dimensional views of the horizontal wind inside tropical cyclones, capturing the vertical wind shear and regions of wind convergence and divergence, particularly well in the glaciated part of the storm;
- WIVERN can estimate the maximum winds in the inner core when multiple close-in-time overpasses are available, thereby capturing the intensification of a tropical cyclone;
- WIVERN can profile the mass of a tropical cyclone anvil as a function of distance from the eye, thus revealing the mechanisms behind its formation.

Corresponding author: Alessandro Battaglia, alessandro.battaglia@polito.it

Abstract

The WIVERN concept is set to enhance the global tropical cyclone observing system. Operating from a 500 km near-polar orbit, the radar 3 m diameter conically scanning antenna with off-nadir pointing provides an 800 km swath, with vertical resolution of 600 m and horizontal resolution of less than 1 km. With quasi-daily global coverage, WIVERN will measure in-cloud tropical cyclone winds up to 40 m/s without any Nyquist ambiguity from 1 km above the surface to the upper troposphere, spanning horizontal scales from 1 to 800 km.

A WRF hindcast study at 1.5 km grid spacing for Hurricane Milton, the most powerful hurricane of the 2024 season, is used as a test bed to showcase WIVERN products and science potential. The WRF simulation reproduces well the trajectory of the hurricane and its maximum wind intensity, which increased by 78 knots in the 24-hour period from 00:00 UTC October 7 to 00:00 UTC October 8.

Full end to end WIVERN simulations demonstrate that: 1) WIVERN will provide a three-dimensional view of the horizontal wind inside cyclones, in particular capturing the vertical wind shear, the upper level divergences and the in-cloud circulations inside the anvil produced by the hurricane convective towers, and some of the inflow and outflows in the lower layers of the atmosphere (1-2 km); 2) In presence of close-in-time overpasses WIVERN has the potential to detect the intensification of cyclone by estimating the maximum winds in the inner core; 3) WIVERN will profile the tropical cyclone ice mass as a function of the distance from the eye, which will help in shedding light into the anvil formation and dissipation mechanisms for such weather systems.

1 Introduction

A Tropical Cyclone (TC) is "any low pressure system having a closed circulation and originating over a tropical ocean" (Houze, 2010) with peak wind speeds exceeding 33 ms^{-1} in severe TCs (hurricanes and typhoons). They play a paramount role in the Earth's radiation budget and in the water cycle by transporting heat and moisture from the tropics to the mid-latitudes and by releasing huge quantities of latent heat (Emanuel, 2001, 2003; Scoccimarro et al., 2011). Furthermore they have tremendous societal impacts, causing widespread destruction due to strong wind and excessive amounts of rainfall when they make landfall (Klotzbach et al., 2018) but also due to swell waves radiating out from the TC core (Yurovskaya et al., 2023). Once generated, TCs can intensify into a fully destructive stage in less than a couple of days (Zehr et al., 1976).

Tropical cyclogenesis is an upscaling process whereby convective-scale dynamics locally add energy and vorticity to a large-scale cyclonic disturbance in regions where synoptic conditions are conducive to convective development. There is still no broad consensus on how to understand and predict tropical cyclogenesis (Emanuel, 2003). Several studies have found that environmental vertical wind shear (usually defined in the environment surrounding the TC between 200 and 850 hPa due to limited wind observations within the middle troposphere (Gray, 1968)) is the main driver of tropical cyclogenesis, intensification, and dissipation, due to its ability to induce kinematic and thermodynamic asymmetry (Thatcher & Pu, 2011; Schenkel et al., 2020; Wadler et al., 2022; Rios-Berrios et al., 2024, and references therein). In this context, low vertical shear allows for a vertically aligned vortex, maintaining the coherence between the lower and upper tropospheric circulation. This alignment is essential for sustaining deep convection near the storm center and fostering a symmetric inner-core structure, which facilitates efficient latent heat release and intensification processes. On the other hand, moderate to strong shear can tilt the vortex, displace convection from the center, and disrupt the upper-level outflow, ultimately suppressing intensification or even causing weakening (Frank & Ritchie, 2001).

However, TC intensity change is generally governed by more complex, intertwined, multi-scale processes (Judt & Chen, 2016). The prediction of TC rapid intensification and the mechanisms controlling this process remain areas of active research (for example, Liu et al. (2025) recently suggested that the size of the TC has a significant impact on its intensification). The environmental effects that govern the evolution of TC intensity (e.g. ambient humidity, sea surface temperature, ocean mixed layer depth and wind shear) have been thoroughly discussed in the literature and their respective contribution are still the subject of debate (see, for example, Emanuel et al. (2004); Hendricks et al. (2010); Wang et al. (2025)). Conversely, internal dynamical processes such as eyewall and rainband convection, which release latent heat, can be a key factor in TC intensification, but are not well understood (Rogers et al., 2013; C.-C. Wu et al., 2016). Based on a database of more than 8,000 high-resolution CloudSat overpasses of TCs (Tourville et al., 2015)) and by exploiting the fact that the cloud Ice Water Content (IWC) derived from cloud spaceborne radars such as CloudSat or EarthCARE CPR can be used as a proxy for latent heating, S.-N. Wu & Soden (2017) have demonstrated that strengthening storms have 20% higher IWC than weakening storms, especially in the midtroposphere near the eyewall (see their Fig. 2). Since rapid intensification is often associated with the reorganization of the TC mesoscale cloud and precipitation structures, it is essential that models are able to predict such structures accurately and for the right physical and dynamical reasons.

The description of the secondary circulation of a mature TC is also uncertain. Several foundational studies suggest that it consists of a boundary layer inflow that first rises in the deep convective towers of the eyewall before turning outward to form the cirrus cloud shield just below the tropopause (Houze, 2010). In this widely accepted view, updrafts within the outer rainbands are not contributing to the primary outflow (see Fig. 1 in Nolan et al. (2025)). Novel TC model simulations performed by Nolan et al. (2025) reveal a different picture from the examination of the mass and moisture budgets of the cirrus outflow shield: a significant fraction of the dry air mass flux (widely varying but around 50%) and even larger fraction of the condensate in the outflow is supplied by deep convection in the surrounding rain-bands (see Fig. 8 in Nolan et al. (2025)). This pinpoints at the importance of the rainband convection in controlling the size and thickness of the outflow clouds, which is a key driver for estimating storm intensity.

Significant progress has been made in the monitoring of TCs from space in recent years and will be extended in the upcoming years (Ricciardulli et al., 2023). While in-situ and aircraft remote sensing data allow a dense monitoring of TCs in the Atlantic Ocean (Holbach et al., 2023), satellite observations remain essential in the other basins and away from the coasts in the Atlantic. In brief this include:

- SAR systems, capable of mapping surface winds at very high resolution ($\sim$3 km) without suffering from high wind or rain-induced saturation and of capturing features such as the eyewall (and its circulation), outflow boundaries, and rainbands (e.g. Mouche et al. (2019); Avenas et al. (2023)).
- C and K_u-band scatterometers and radiometer systems with frequency bands from L to X (e.g. SMOS, SMAP, AMSR-2) providing winds at the surface but at coarser resolutions, TC center location, intensity, radial and rotational structure. The new generation of scatterometers with cross polarization will improve measurements for extreme hurricane winds.
- microwave imagers/sounders (e.g. GMI, SSMIS and, in the future, CIMR and MWI) providing, in addition to surface properties (wind speed and sea surface temperatures), information about precipitation, water vapour and cloud contents (but with very coarse vertical resolution). This also includes a new generation of small and cube satellites (e.g. TROPICS and TEMPEST).

- Doppler wind lidars with ESA-Aeolus2 expected to fly in the next decade after Aeolus demonstrated the potential of spaceborne Doppler lidar for observing clear air dynamics around the cyclones.
- K_u-K_a-W band spaceborne radars profiling cloud and precipitation vertical structure (Battaglia et al., 2020a) but with very limited coverage particularly for W-band radars (EarthCARE cloud profiling radar is nadir looking).
- Geostationary sensors monitoring the rapid temporal evolution of convective features and exact location of the storm and producing atmospheric motion vectors for storm cloud tops. Resolutions down to 1-2 minutes are becoming soon operational for targeted areas.

Despite this plethora of instruments, there is a lack of observations for the global continuous monitoring of the three dimensional structure of the winds and of the hydrometeors inside TCs. The Wind Velocity Radar Nephoscope (WIVERN) mission, equipped with a groundbreaking Doppler radar (Illingworth et al., 2018; Battaglia, Rizik, et al., 2025; ESA WIVERN Team, 2025), promises to fill this gap in the observing system and capture, for the first time, the three-dimensional dynamics and microphysical structure of all types of storms on Earth below 86° latitude. This includes horizontal winds in stratiform regions, updrafts and downdrafts in convective cells, and the mass of condensed water above the freezing level. The mission will cover a more than 800 km wide swath with quasi-daily revisit times. WIVERN measurements will be collected at 1 km intervals along its conically scanning beam and will be vertically resolved with a resolution of 600 m.

This work aims at demonstrating that the WIVERN mission will achieve two major goals. First, WIVERN will provide in-cloud wind measurements, thus bridging between the surface (as provided by SARs, scatterometers and radiometers) and the upper troposphere winds (as provided by geostationary sensors). In less than two minutes per overpass, the WIVERN Doppler radar will provide a full three-dimensional map of horizontal winds within TCs where clouds exceeding -18 dBZ are present. The amount of profiles collected by WIVERN in a single overpass inside the TC will be equivalent to that acquired by a research aircraft equipped with a nadir-looking radar sampling continuously for about four days. Second, WIVERN will simultaneously provide a unique, three-dimensional view of clouds and precipitation across the entire storm, complementing in the TC glaciated part what TRMM and GPM K_u and K_a band precipitation radars have provided inside moderate and heavy precipitation regions (Battaglia et al., 2020b).

The theory underpinning the concept is outlined in Sect. 2. Then simulations of WIVERN overpasses are thoroughly discussed (Sect. 3). Conclusions and recommendations are drawn in Sect. 4.

2 Methodology

This section outlines the rationale, methodology and underpinnings of the study. The WIVERN radar operates from a 500 km near-polar orbit a 3 m diameter conically scanning antenna with off-nadir pointing leading to an incidence angle of approximately 42°. This configuration provides coverage across an 800 km swath, with vertical resolution of 600 m, and horizontal resolution of approximately 1 km. With quasi-daily global coverage, WIVERN will enable the measurements of in-cloud TC winds from ≈ 1 km above the surface to the upper troposphere, spanning horizontal scales from 1 to 800 km.

Throughout ESA Phase 0 and A studies, a comprehensive end-to-end simulator was developed to reproduce WIVERN observables from atmospheric and surface targets, incorporating successive refinements (Rizik et al., 2023; Battaglia, Rizik, et al., 2025; Manconi et al., 2025) to the initial framework proposed in Battaglia et al. (2022). The schematic of Fig 2 illustrates the main steps, inputs and outputs of the simulator.

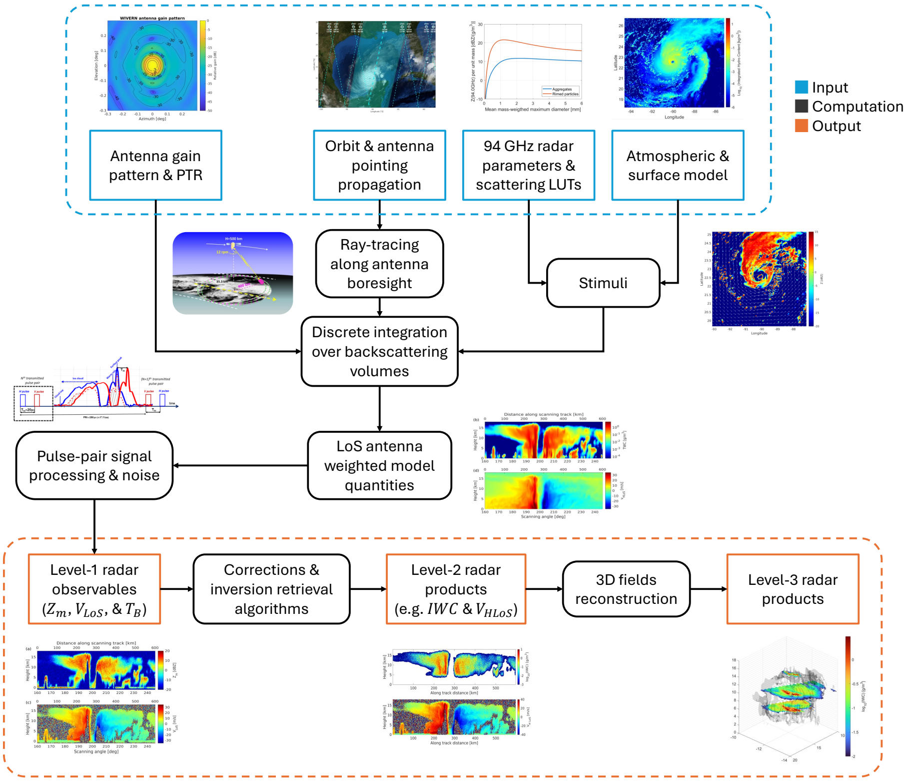

Figure 1. Flow chart of the WIVERN mission end-to-end simulator architecture.

In brief, the simulator uses outputs from cloud-resolving models, such as the Weather Research and Forecasting (WRF) mesoscale numerical weather prediction system, which provide three-dimensional distributions of wind, hydrometeors, temperature, and water vapor (see Sect. 2.1). These quantities are then converted into 94 GHz radar properties, or stimuli, including extinction, scattering, backscattering coefficients, single scattering albedo, and asymmetry factors via 94 GHz scattering look-up tables that are built (details in Battaglia et al. (2022)).

Each footprint is illuminated by the WIVERN antenna and scanning pattern for any given orbit, computing the Level 1 radar observables [line-of sight (LoS) Doppler velocity (v_{LoS}), radar reflectivity factor (Z) and brightness temperatures in the H- and V-polarized channels ($T_b^{H,V}$] taking into account the sampling rate, the sensitivity and the specific pulse scheme of the instrument (details in Battaglia, Rizik, et al. (2025)). Details about how the simulations and an example of the outputs are discussed in Sect. 2.2.

From the Level-1 radar observables a variety of Level-2 products can be derived (ESA WIVERN Team, 2025). Here, the focus is restricted to the Horizontal wind along the horizontally-projected Line of Sight (HLoS) and the IWC. Before any estimate of Level-2 products can be made, several corrections are applied to the reflectivity and LoS Doppler velocity fields.

Reflectivities are first noise subtracted similarly to what is done for CloudSat and EarthCARE (Marchand et al., 2008), then they are corrected from the attenuation due to water vapor and oxygen, estimated from the temperature and pressure profiles, and from the ghost echoes associated with the polarization diversity technique employed by

WIVERN (Rizik et al., 2023). Finally, the range bins contaminated by surface clutter echoes are filtered out (Scarsi et al., 2024; Manconi et al., 2025).

Biases in the LoS Doppler velocity due to non-uniform beam filling and wind shear inside the radar volume are corrected for using gradients of the reflectivity and of the velocity fields (Battaglia, Rabino, et al., 2025). The contribution of the sedimentation velocity of the hydrometeors on the LoS Doppler velocity is estimated and corrected based on statistical relations with the measured reflectivity (ESA WIVERN Team, 2025). The variability of the reflectivity and Doppler velocity fields together with brightness temperature depressions associated with dense ice are used in a U-NET neural network (Mustich et al., 2025) to filter out convective regions where updrafts have significant contribution to the measured LoS doppler velocity.

The HLoS Velocity (V_{HLoS}) product is then computed in stratiform regions where vertical winds can be neglected ($w \approx 0$). Then, V_{HLoS} is computed from trigonometry as:

$$V_{HLoS} = \frac{V_{LoS} - (\cancel{w} + V_T^D)\cos(\theta_I)}{\sin(\theta_I)} \approx 1.5\ V_{LoS}^{L2A} - 1.1\ V_T^D \qquad (1)$$

where $\theta_I \approx 42°$ is the WIVERN beam incidence angle, V_{LoS} is the measured LoS velocity (corrected for mispointing and NUBF effects) and v_T^D is the reflectivity weighted terminal velocity of hydrometeors that can be derived by $Z-v_T^D$ relationships (Kalesse & Kollias, 2013).

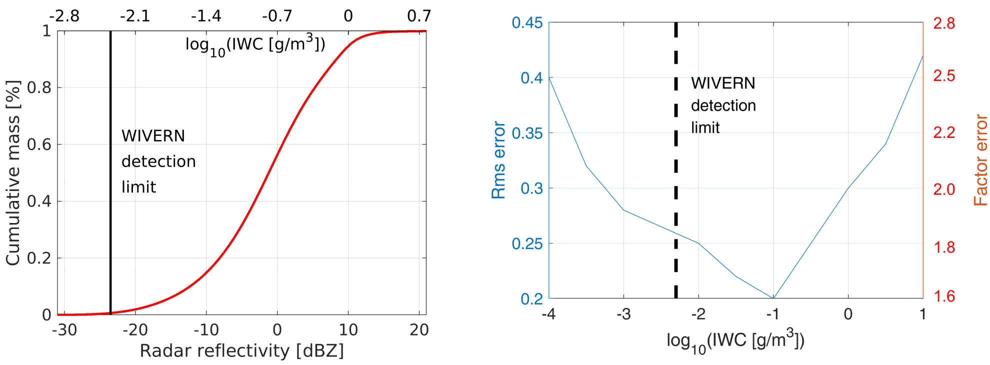

Figure 2. Left panel: cumulative mass for ice clouds as a function of the radar reflectivity factor as computed from the CloudSat 2B-CWC-RO IWC product for the entire year 2008. Right panel: root mean square error for $\log_{10}(IWC[g/m^3])$ according to Protat et al. (2007) as a function of the IWC (in log-units).

Established Z-IWC relationships (Protat et al., 2007) are adopted for the inversion from Z to IWC. With WIVERN expected sensitivity of about -23.5 dBZ at 1 km integration (ESA WIVERN Team, 2025), an IWC detection limit of about 0.005 g/m^3 is foreseen. Note that this limit accounts for 99.3% of the mass of ice clouds (see left panel in-Fig. 2) as computed by using CloudSat 2B-CWC-RO IWC product statistics for the entire 2008. No retrieval is attempted in convective columns, identified by model vertical winds that exceed in absolute value 2 m/s.

The retrieval error is dominated by retrieval errors (i.e. the uncertainties associated to translating the radar backscattering signal int the IWC geophysical parameter). Following the findings by Protat et al. (2007) for a 94 GHz operating in the tropics, the noise function reproduced in the right panel of Fig. 2 for the $\log_{10}(IWC)$ is used to inject noisiness into the retrieval. This root-mean-square (rms) error of the $\log_{10}(IWC)$ correspond to a multiplicative error for the IWC with a factor, $f \equiv 10^{rms}$, indicated on the right y-axis. Consequently, for each WIVERN backscattering volume, IWC is sampled from a log-normal distribution, whose mean value, $\langle IWC \rangle$, corresponds to the value derived via the Z-IWC and the standard deviations is computed as half the difference $f\langle IWC \rangle - \langle IWC \rangle / f$.

From these two Level-2 products (horizontal LoS wind and ice mass) which are defined along the WIVERN rays (and therefore represent a cloud of sparse points across the TC volume), Level-3 three-dimensional gridded fields can be reconstructed, following the methods explained in Sections 2.4 and 2.5.

2.1 WRF simulations

The NWP model adopted in this study is Weather and Research Forecasting (WRF) a next-generation mesoscale numerical weather prediction system designed to serve both operational forecasting and atmospheric research needs (Powers et al., 2017; Skamarock et al., 2019). WRF is suitable for a broad spectrum of applications across scales ranging from meters to thousands of kilometers. In this study WRF model version 4.6.1 has been adopted with 2 two-way nested domains at 4.5, and 1.5 km grid spacing.

Figure 3. WRF domains at 4.5 and 1.5 km grid spacing

The innermost domain at 1.5 km grid spacing is based on the WRF model moving-nest approach (Gill et al., 2004). This option allows one of the nested domains to follow a feature of interest, such as a tropical cyclone, convective system, or any other moving weather phenomenon. This enables higher-resolution modeling in the area of interest throughout the simulation, conserving computational resources while improving forecast accuracy in critical regions. The initial and boundary conditions are provided by ERA5. The ERA5 dataset is a cutting-edge global climate reanalysis product developed by the ECMWF as part of the Copernicus Climate Change Service (C3S). It represents the fifth generation of ECMWF reanalysis efforts, succeeding the ERA-Interim dataset. ERA5 features significant enhancements compared to ERA-Interim, including improved spatial and temporal resolutions, with a grid resolution of around 31 kilometers and a temporal resolution of 1 hour (Hersbach et al., 2020; Soci et al., 2024). ERA5 provides comprehensive data coverage from 1940 to the present, with updates occurring every two months.

The WRF model study simulation is initialized on 5 October 2024 and it runs until 11 October 2024 with 6 hourly boundary conditions provided by ERA5 analysis. Concerning the WRF model setup, the Rapid Radiative Transfer Model for GCMs (RRTMG) shortwave and longwave schemes (Iacono et al., 2008) are used for radiation, while the Rapid Update Cycle (RUC) scheme is chosen as a multi-level soil model (6 levels) with higher resolution in the upper soil layer (Smirnova et al., 1997, 2000; Benjamin et al., 2004). No cumulus scheme is activated in the two domains (4.5 and 1.5 km grid-spacing), because the grid-spacing enables to resolve the convection dynamics explicitly. The microphysics is simulated using Thompson hail/graupel/aerosol aware scheme (Thompson & Eidhammer, 2014) which includes ice, snow, graupel and hail processes suitable for high-resolution simulations, considers water- and ice-friendly aerosols. Aerosol-ice friendly aerosols are atmospheric particles that are capable of initiating the formation of ice crystals in supercooled cloud droplets (i.e., droplets that remain liquid below 0°C). These aerosols promote heterogeneous ice nucleation, a process important in cloud microphysics and climate modeling. This microphysics computes two-moment prognostics (mass and number concentration)for graupel and hail, including a predicted density graupel category. In terms of turbulence closure, the vertical turbulent mixing is operated by the Yonsei University (YSU) scheme (Hong et al., 2006) is based on a turbulent kinetic energy, while the horizontal mixing is operated by the 1.5-order turbulent kinetic energy (TKE) prediction (Fiori et al., 2010, 2011, 2017). Hasan et al. (2022), which prognoses TKE (a second-moment quantity), but still uses diagnostic relations (like gradient-diffusion assumptions) to compute fluxes, found that WRF has significant implicit numerical dissipation, resulting into a weaker hurricane and a weaker rapid intensification. This is due to the fact that the pressure gradient discretization is only 2nd order, which smooths the response to localized heating anomalies associated with convective bursts. In this study the numerical dissipation is counteracted by reducing the Smagorinsky and Turbulent Kinetic Energy (TKE) coefficients have been reduced to 12.5 percent of their default values, namely $c_s = 0.25$ and $c_k = 0.15$. The Smagorinsky Coefficient determines the intensity of eddy viscosity based on the local strain rate of the flow, while the TKE coefficient relates turbulent fluxes to TKE and stability of the atmosphere.

2.1.1 WRF results

The WRF predictive capability for the Milton hurricane is assessed by the comparison between the National Hurricane Center (NHC) best track and the WRF predicted one, as well as by the comparison between the observed and predicted maximum 10 m wind speed. When the WRF automatic moving nest is employed, the model writes the vortex center location, with minimum mean sea-level pressure and maximum 10-m winds making easier the comparison with observational data.
The following figure shows the comparison between the 6-hourly time interval NHC best track and the 15 minutes time interval WRF track for the time interval from 6th October 2024 00UTC and 10th October 2024 00UTC. The overall agreement is very good even if WRF model experiment anticipates the landfall over Florida of about 6 hours earlier than observed. Also in terms of intensity the WRF model experiments capture pretty well the RI intensification period between 12UTC on 6th October and 00UTC on 8th October 2024. It is worth to mention that the observed Milton was reaching category-5 intensity while the simulated one "only" category 4, but still the agreement is significant and supportive of subsequent usage for testing WIVERN performances.

2.2 Spaceborne WIVERN Doppler radar simulations

The WIVERN radar simulations are run using the WRF outputs for Hurricane Milton, covering the period of time from 6/10/2024 at 10:00 UTC to 8/10/2024 at 00:00 UTC, in intervals of 1 hour (39 hours in total). Each of the 39 snapshots of the hurricane is used to provide to the simulator a spatial domain of 1250×1250×20 km^3 centered around

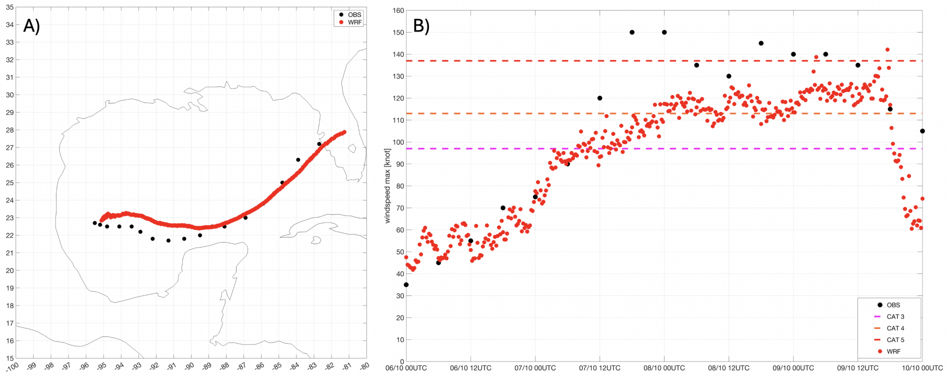

Figure 4. Panel A): comparison between the NHC best track (6 hourly data) and the WRF model vortex track with 15 minutes time interval. Panel B): comparison between the NHC maximum wind speed (6 hourly data) and the WRF model instantaneous maximum wind speed with 15 minutes time interval

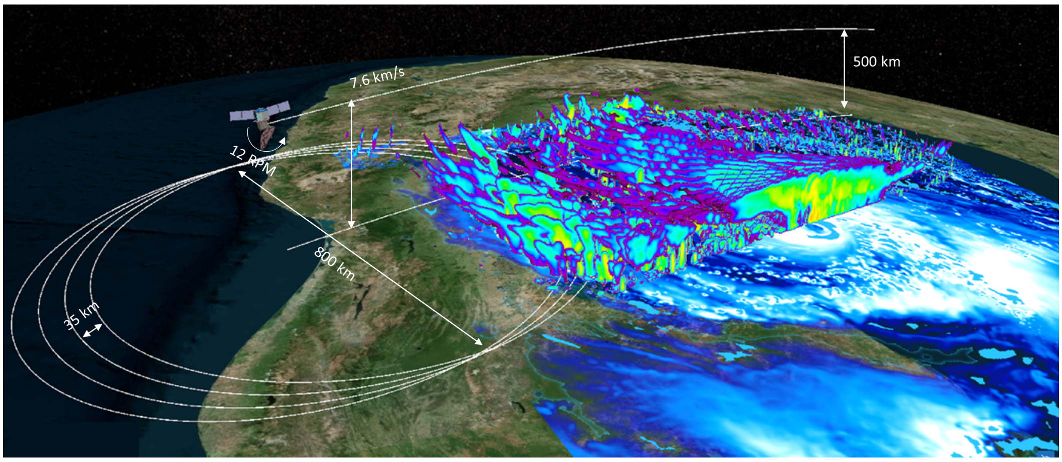

Figure 5. Illustration of the scanning geometry envisioned for the WIVERN mission. For representation purposes, dimensions are not to scale. The right edge of WIVERN swath is just crossing the hurricane eye. The Level-1 reflectivity product is illustrated across WIVERN swath whereas the total hydrometeor content field is depicted with bluish colors (white indicate high contents, dark blue small contents) on the easternmost part of the hurricane, outside WIVERN swath.

the cyclone eye, with a horizontal resolution of roughly 1.5 km and vertical resolution of approximately 500 m (but finer at heights lower than 3 km).

The orbit and pointing of WIVERN are propagated for the full duration of the available Milton WRF data. Realistic orbital parameters for the planned WIVERN sun-synchronous orbit are used, with an inclination of 97.4 degrees, altitude of roughly 500 km, and a Local Time of Ascending Node (LTAN) of 6 AM. During the 39-hour propagation period, each overpass where the satellite ground track is closer than 400 km from the cyclone eye is registered as a valid pass and subsequently adopted for simulation with the corresponding WRF-simulated conditions. Each simulation spans 200 seconds (i.e. 40 complete antenna rotations) centered around the time of minimum distance between the satel-

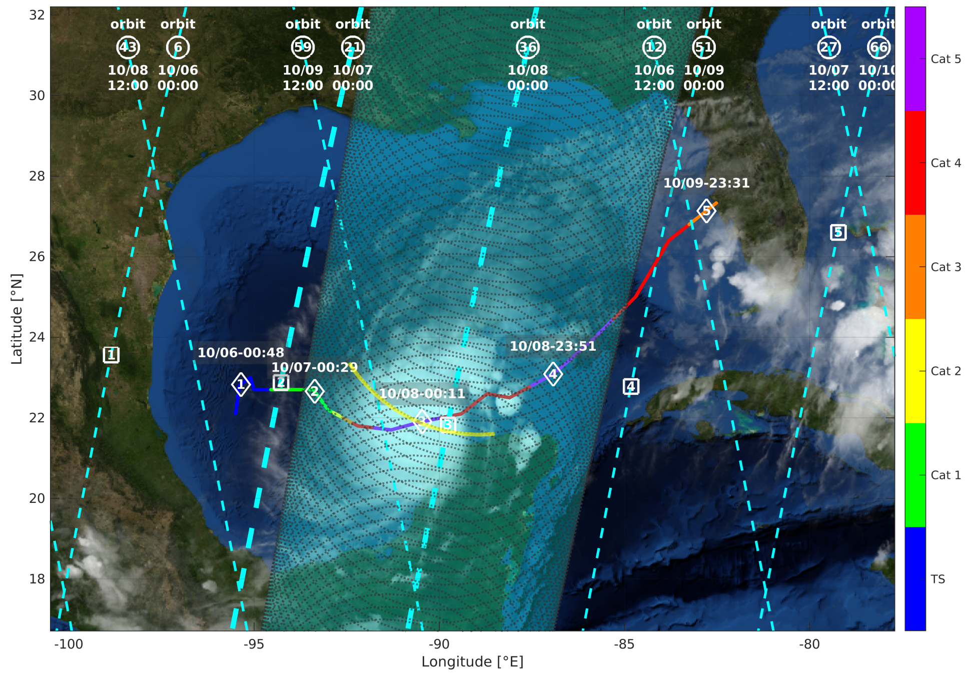

Figure 6. The path of Hurricane Milton from 10/06/2024 to 10/10/2024 with its color-coded intensity, as reconstructed by NOAA. The nine WIVERN satellite ground-tracks passing through the Gulf of Mexico during these four days are indicated with cyan dashed lines. Five orbits pass within 400 km from the hurricane centre with the five positions of the hurricane eye and the closest satellite ground-track indicated by diamonds and squares, respectively. The WIVERN scanning pattern is shown only for the 10/08 descending pass, with the sector of the scan plotted in Fig. 7 highlighted in yellow.

lite ground-track and the hurricane eye. During 40 rotations the satellite advances 1400 km so that a complete coverage of the hurricane is provided both by the forward and backward views (Fig.5). An example of the simulations is provided in Fig. 6 and 7.

In Fig. 6, an example of successive overpasses across the path of Hurricane Milton is shown, from the 5th to the 10th of October. Within this time period, Milton originated as a tropical storm in the west part of the Gulf of Mexico and made landfall in Florida as a category 3 hurricane. In between, it went through a rapid intensification (from category 2 to category 5) just in a single day (the 7th of October). The dashed cyan lines drawn in Fig. 6 correspond to the WIVERN satellite tracks within the Gulf of Mexico region, adopting real orbital parameters planned for the mission. Out of the ten tracks, five are passing within a 400 km distance from the TC eye; this ensures adequate coverage of the storm life cycle. These five overpasses are identified with numbered squares and diamonds, each corresponding to the minimum distance positions of the satellite ground track and of the TC eye, respectively. Of particular interest for this study are the overpasses labeled as (2) and (3), which straddle Milton rapid intensification period.

In Fig. 7 the three main observables and three most relevant WRF model quantities are plotted for a section of the scan passing near the cyclone eye, highlighted in yellow for overpass with label (3) in Fig. 6. In panels (a) and (b), a cross-section of the eye and eyewall of the cyclone is clearly identifiable. The eye appears as a column of generally low hydrometeor contents with near-zero wind speed, while the eyewall and rainbands exhibit high total water content (TWC), leading to significant attenuation and eventually total extinction of the measured reflectivity signal (Z_m). Shallow convection cells can also be seen at the beginning of the scan, on the left of the plots. As expected, Z_m generally correlates with TWC: at altitudes above ∼5 km (roughly the freezing level), extensive anvil clouds with high ice content are evident, while at lower levels the rainbands outside of the eyewall are clearly visible with high content of hydrometeors (see also terminal velocity of the hydrometeors under the freezing level in panel (f)). Panels (c) and (d) highlight the dominance of horizontal winds in the Doppler velocity field, which exhibits the typical dipole structure associated with cyclonic circulation, characterised by opposite wind directions on either side of the eye. In panel (f), convective updrafts (blue regions) are apparent within the eyewall, while below the freezing level, vertical velocities are enhanced by the downward motion of rain. Regions of deep convection typically correspond to lower brightness temperatures, as seen in panel (e) in correspondence of the eyewall, rainbands and minor shallow convection cells.

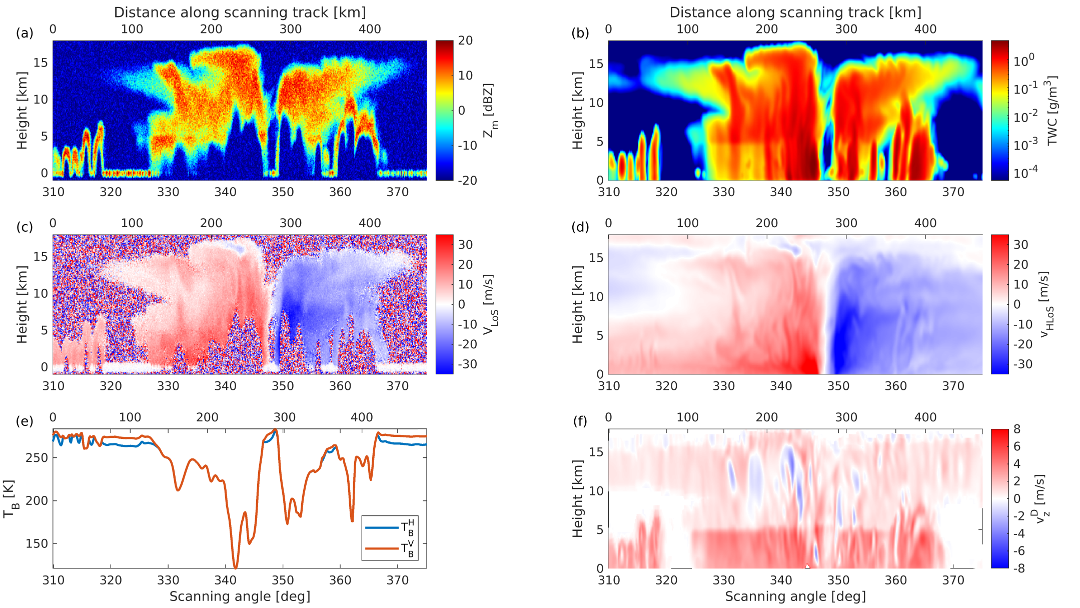

Figure 7. Curtain plots for the scan sector highlighted in yellow in Fig. 6. The left column displays the main observable, from top to bottom: (a) measured reflectivity (Z_m), (c) Doppler velocity (V_{LoS}), and (e) vertical and horizontal brightness temperatures (T_B^H and T_B^V). The right column shows antenna-weighted "true" quantities along the line-of-sight from the WRF model: (b) total water content (TWC), (d) horizontal component of the line-of-sight (LoS) wind (V_{HLoS}), and (f) vertical LoS wind component combined with the hydrometeor terminal velocity (V_Z^D).

2.3 WIVERN scanning pattern

WIVERN scanning pattern is a distinctive feature of the mission, offering several advantages (Fig. 9).

- The swath width is about 800 km, unprecedented for cloud and precipitation radars. The TRMM/GPM radars have swaths up to 250 km, with no sensitivity to clouds and their footprints are larger than 4 km. The INCUS mission will have a 10 km swath, but with similarly limited sensitivity to clouds and footprints exceeding 3 km. Cloudsat/EarthCARE CPR have much narrower swaths of 1.6 km and 750 m, re-

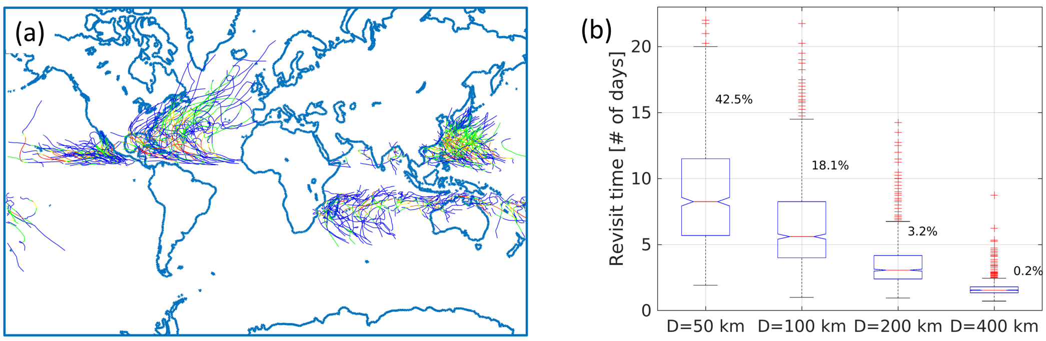

Figure 8. Panel (a): ground-tracks of the last 35 years TC that reached at least Category 1 level (maximum velocity above 33 m/s) during their lifetime (Knapp et al., 2010). The colour for the tracks indicate different TC intensities (blue for tropical storm; green, yellow, orange, red, violet for TC from category 1 to category 5, respectively. Panel (b): revisit time (expressed in number of days) for the WIVERN ground-track to pass within a given distance (D) from the TC eye. In each boxplot, the central mark indicates the median, the bottom and top edges of the box the 25th and 75th percentiles, respectively. The whiskers indicate the range of non outliers whereas outliers are shown as '+' symbols. The percentage numbers express the probability of missing completely the TC.

spectively. WIVERN effectively bridges the gap between the km-scale resolution (footprint size) and mesocale coverage (swath width).

- Moving at about 500 $\mathrm{km\,s^{-1}}$, the footprint sweeps through an unprecedented volume of the atmosphere. With a sampled area of about 500 $\mathrm{km^2s^{-1}}$, it has unparalleled sampling capabilities for a km-scale sensor. By comparison, EarthCARE and CloudSat CPR sample the troposphere sweeping areas at rates of 5.5 $\mathrm{km^2s^{-1}}$ and 11 $\mathrm{km^2s^{-1}}$, respectively, while the INCUS mission achieves 70 $\mathrm{km^2s^{-1}}$. In a nutshell, in one week WIVERN will sample as much as EarthCARE does in a year, and as much as INCUS does in a week, WIVERN does in just a day.
- WIVERN measurements have azimuthal diversity, a critical feature for retrieving vector winds (i.e. the zonal and meridional components), depending on their location within the swath. As shown in Fig. 9, the blue and red cells near the satellite ground track and at the edges of the swath have limited azimuthal diversity; accordingly, good retrievals are expected primarily for the along-track and cross-track components, respectively. In contrast, the green cell is characterised by looks with a wide range of azimuth angles, allowing the reconstruction of the horizontal wind vector.
- The number of 1 km along-track measurements in each $10\times10\,\mathrm{km^2}$ pixel is much higher near the edges of the swath than in the centre, with a very sharp gradient in the 50 km closest to the swath edge (upper inset in Fig. 9). In the central part of the swath, the distribution is bimodal, with either no measurements or about 10. This reflects the sparseness of the scans in this region.
  On the other hand, near the swath edges, within a 20 km wide strip, the sampling is excellent, each $10 \times 10\,\mathrm{km^2}$ pixel contains between 20 and 56 measurements. This almost full coverage at the swath edges will allow to use WIVERN as a calibrating reference system for other sensors.

The sparse WIVERN sampling can be used to produce two swath products:

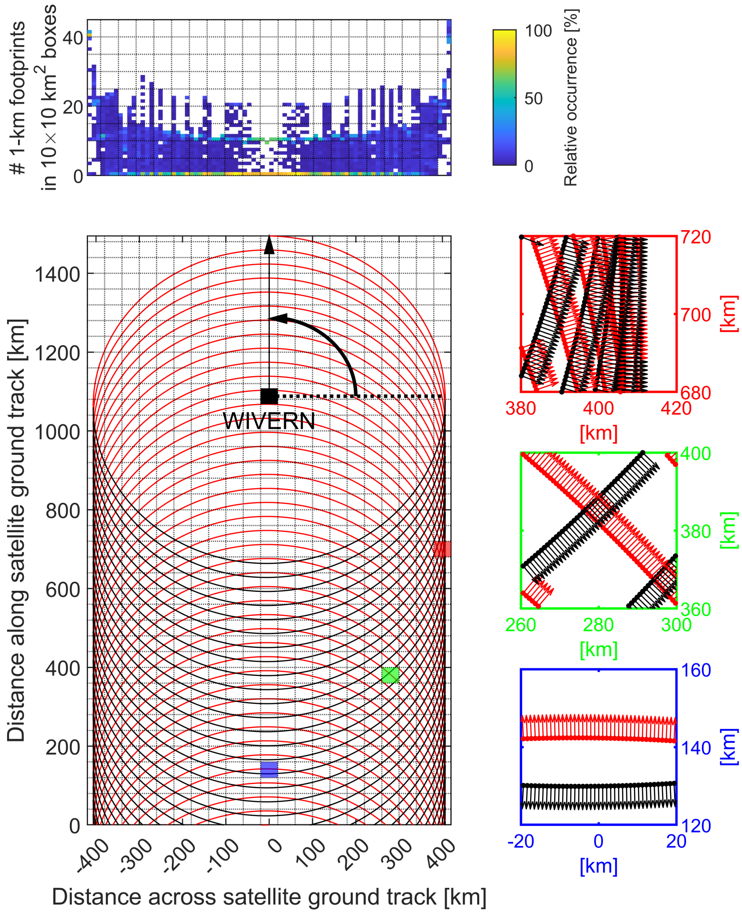

Figure 9. WIVERN scanning measurements at a fixed altitude. The satellite is assumed to move upward at 7.0 km s^{-1} while scanning an 800 km swath at 12 rpm. The radar footprint is about 1 km. Red and black dots indicate forward and backward views, respectively. The three insets on the right show zoomed-in views of the sampling within the green, cyan and pink cells, each covering a 40×40 km^2 region located at the swath edge and centre. Red (black) arrows represent the HLoS directions for each available measurement in the cell for the forward (backward) views. The top inset shows the relative occurrence of 1 km along-track averaged measurements in each 10 × 10 km^2 pixel as a function of distance from the ground track.

1. A three-dimensional Horizontal Wind Vector Field, which contains the reconstructed three-dimensional horizontal wind field across the full swath with a resolution of $10 \times 10 \times 0.5$ km^3 (Sect. 2.4).
2. A three-dimensional Stratiform Ice Mass Field, which contains the three-dimensional distribution of the ice mass also at a resolution of $10 \times 10 \times 0.5$ km^3 (Sect. 2.5).

2.3.1 WIVERN Tropical Cyclone Sampling

A systematic analysis has been conducted to assess how well WIVERN will sample the lifecycle of TCs. Statistics based on more than 1,350 tracks extracted from the database of the last 35 years TCs reaching at least Category 1 (i.e. 64 knots, Knapp et al. (2010), Fig. 8a) coupled with simulations of the WIVERN orbit have been exploited to compute what is the distribution of the mean revisit time within a certain distance

D from the TC eye for TCs lasting at least 3 days (99% of them). Results are presented in Fig. 8b in the form of boxplots for four values of D from 50 to 400 km. The study reveals that 1.55 is the median (1.35 and 1.8 are the 25^{th} and 75^{th} percentiles) number of days required for the WIVERN track to revisit a TC within a 400 km distance from the TC centre (fourth boxplot in Fig. 8b). This guarantees that WIVERN will be able to map winds inside at least half of each TC more frequently than every other day. Note that only 0.2% of the TC are completely missed. In comparison, a nadir-pointing radar (like CloudSat or EarthCARE) would typically provide only a 2D curtain within 50 km of the eye every 8.3 days (5.7 and 11.5 are the 25^{th} and 75^{th} percentiles of the distribution, first boxplot in Fig. 8.b) and would miss the TC 42.5% of the time.

Finally note that with an average of about 42 TCs per year of Category 1 or more there will be on average about 17, 36 and 290 overpasses per year of a polar orbiting satellite like WIVERN within 25, 50 and 400 km, respectively. This is equivalent of having hundreds of TC dedicated field campaigns with aircrafts every year. When considering all TCs lasting at least one day (on average 102 per year), there will be on average about 32, 63 and 512 overpasses per year within 25, 50 and 400 km,

Tridon et al. (2023) simulated WIVERN data using CloudSat CPR observations within TC and demonstrated that a slant looking 94 GHz radar with the expected WIVERN sensitivity will be able to observe a very large number of winds inside TCs, particularly in the glaciated part of the storm above the freezing level. The probability of obtaining useful Doppler velocity estimates (with an accuracy better than 3 m s^{-1}) is greater than 50% (with respect to the CloudSat reference) up to an altitude of around 11 km, with peak performance between 3 and 9 km. Despite its reduced sensitivity, thanks to its 70 times better sampling, WIVERN will provide 30 times more wind observations than CloudSat cloud observations. Given its 600 m vertical resolution, this implies that WIVERN will measure about 200 million precise winds within TCs per year.

The combination of these two findings reveals that WIVERN has significant potential for mapping TCs in three dimensions and monitoring their evolution, which can last for over a fortnight.

2.4 Three-dimensional horizontal wind vector reconstruction

The three-dimensional horizontal wind vector field can be reconstructed using the WIVERN sampling, through an inversion procedure (Da Silva et al., 2025). The 2D horizontal wind field is recreated at different heights at grid points separated by 10 × 10 km^2. For each node, the two horizontal wind field components are found using an optimization technique based on the standard least squares method(Battaglia et al., 2024). The main idea is to minimize the error between the modeled LoS velocity and the available observations. The modeled LoS velocity is written in terms of the unknown horizontal wind velocity components. Observed data are weighted by an exponential drop based on the distance from the target and a correlation length. Due to sampling sparseness, the correlation length is 20 km near the ground track and decreases exponentially to 5 km at the edge where sampling is excellent. For each grid point, the problem reduces to a linear system, and its inversion allows for the determination of the horizontal components of the wind field by an analytic inverse procedure.

This retrieval procedure is limited by:

- poor radar illumination (regions with no targets or clouds with radar reflectivity below the noise level of -18 dBZ);
- presence of convective cells where the vertical wind component is not negligible;
- azimuth diversity, as shown in Fig. 9, which limits retrievals near the satellite ground track and at the edge of the swath.

2.5 Three-dimensional ice mass field reconstruction

To estimate the three-dimensional ice mass distribution of cloud anvil from WIVERN overpasses, the WIVERN Level-2 IWC sparse retrieval has been first interpolated along each WIVERN ray at a fine vertical sampling of 100 m (using a nearest neighbor interpolation). Then the scattered points (left panel in Fig. 10) are gridded into a three-dimensional uniform grid with 100 m spacing in the vertical and 10×10 km^2 horizontal resolution. The same is done for the model outputs. An example of the model IWC field at 9.6 km is shown in the left panel of Fig. 11 for the case study of Fig. 10.

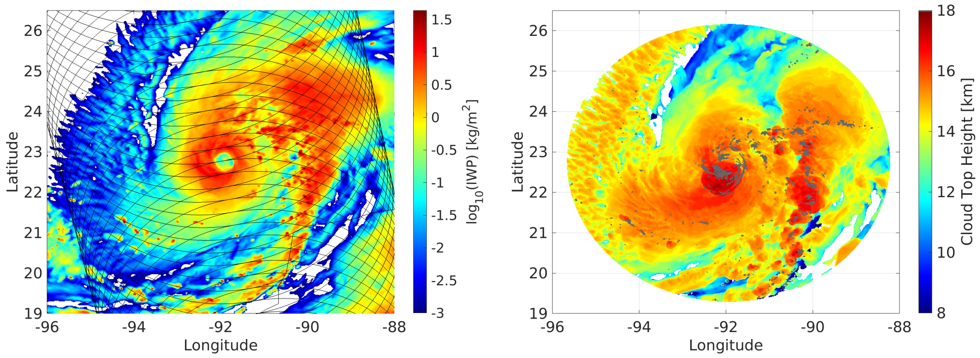

Figure 10. Left panel: WIVERN sampling for an overpass in proximity of the Milton eye on the 7th October at 11UTC. The color is modulated by the ice water path (as indicated in the colorbar legend). Right panel: cloud top height assumed to be detected from geostationary data. Grey-shaded areas correspond to convective columns where no IWC retrieval is attempted.

If multiple WIVERN measurements fall within the same grid box, the IWC attributed to the grid box is equal to the mean in linear units of the different IWC estimates. Zeros values of IWC are attributed to grid boxes located above the cloud top height (assumed to be derived from geostationary auxiliary measurements, right panel in Fig. 10) and 500 m below the freezing level (assumed to be derived from auxiliary ECMWF reanalysis). The corresponding IWC field at 9.6 km is shown in the center panel of Fig. 11.

WIVERN scanning pattern produces gaps, especially near the satellite ground-track (see white pixel in the center panel of Fig. 11). The grid points that are empty (because there is no WIVERN measurement falling inside the grid box) are filled by an interpolation procedure based on the matlab Scatteredinterpolant function (right panel in Fig. 11).

3 Results

The goal of this work is to demonstrate that WIVERN will be able :

1. to provide a three-dimensional view of the horizontal wind inside TCs, in particular capturing the vertical wind shear, the upper level divergences and the in-cloud circulations inside the anvil produced by the hurricane convective towers, and some of the inflow and outflows in the lower layers of the atmosphere (1-2 km);
2. to identify the intensification of a TC by estimating the maximum winds in the inner core from close in time overpasses;
3. to profile the TC ice mass as a function of the distance from the eye, which will help in shedding light into the TC anvil formation and dissipation mechanisms.

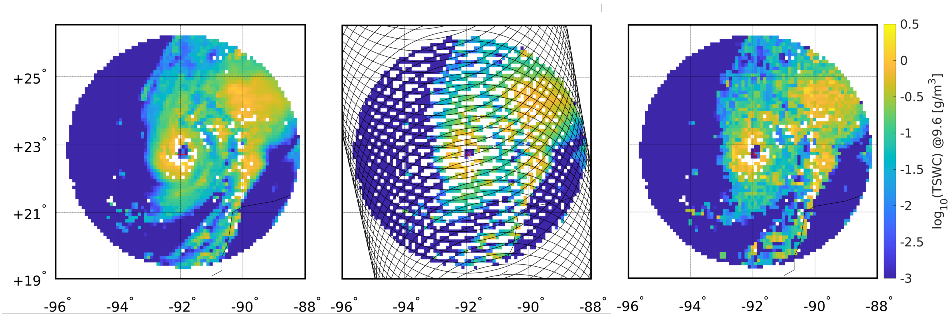

Figure 11. Reconstruction of the anvil IWC three-dimensional field from WIVERN measurements: case study for the 9.6 km level. Results are shown only for a circular area of 400 km radius centered at the TC eye. Left panel: model $\log_{10}(IWC)$[g/m^3] (white pixels inside the 400 km radius correspond to convective towers). Center panel: WIVERN Level-2 IWC gridded at 10×10 km^2 with the antenna boresight line of sight projected at the given height (black line). Right panel: WIVERN retrieved IWC after gap-filling is applied.

The simulations of the evolution of Hurricane Milton are exploited to demonstrate these features.

3.1 Tropical Cyclone Wind Shear Structure

The capability of the WIVERN mission to retrieve wind profiles within the hurricane's inner region and across multiple vertical layers allows for the reconstruction of radial wind patterns and provides new insights into the organization of the storm's inner-core circulation and wind shear distribution.

Thanks to its Doppler radar capabilities and its wide swath scanning, WIVERN can capture the storm internal circulation, particularly well in the glaciated part above 5 km. An overpass on the 7 October at 12 UTC when Hurricane Milton was intensifying toward Category 3 status, corresponding to an ascending orbit with the right edge of the swath located approximately 150 km east to TC center (see Fig. 12), is used to demonstrate the reconstruction of the three-dimensional horizontal wind field, via the technique described in Sect. 2.4. Fig. 12 shows that the horizontal wind structure is accurately retrieved across the different vertical layers, clearly capturing the transition from the cyclonic circulation around the eye, still evident at around 7 km altitude (lower panels), to the divergent outflow at upper levels (top panel). Interestingly there is a good reconstruction even in the lowest layer at H = 3 km even if the coverage is limited (see density of white arrows in the bottom right panel). WIVERN is the only space-borne observing system potentially capable of resolving storm dynamics with this level of detail and spatial coverage. Such observations are crucial, for instance, to determine whether most of the mass detrained into the inner-core region originates from the eye-wall or from the surrounding rainbands (Nolan et al., 2025).

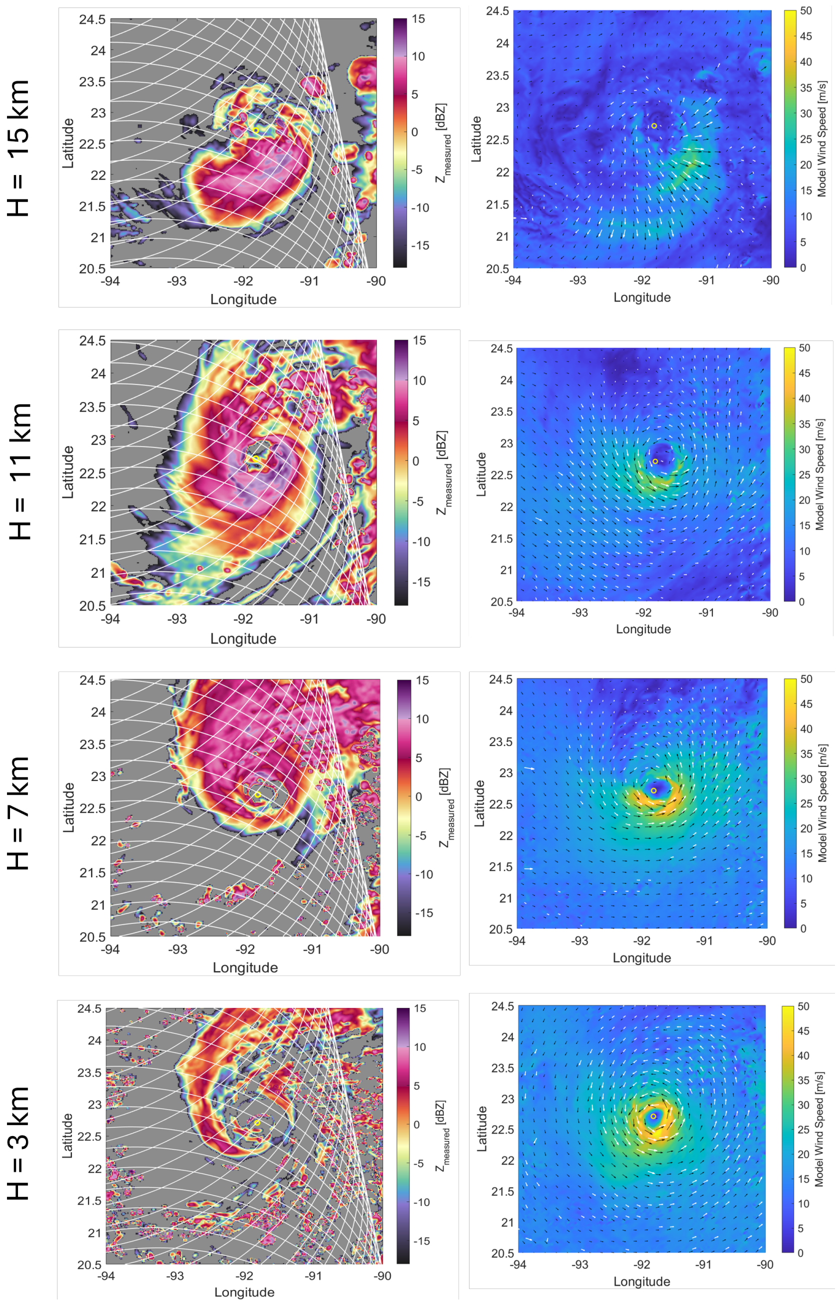

Figure 12. Example of three-dimensional reconstruction of the horizontal winds for Hurricane Milton simulated by the WRF model. Horizontal cross sections at four altitudes are considered: 15, 11, 7 and 3 km, respectively from top to bottom. Left columns: same-height horizontal cuts of simulated reflectivities in dBZ with the WIVERN scanning pattern superimposed. Right columns: model wind field (black vectors) with retrieved winds (white vectors). Note that the retrieved winds correspond to regions where clouds with good reflectivities are present.

To put the internal wind structure of the cyclone in the context of the large-scale environmental conditions, the storm is first partitioned into four shear-relative quadrants (DL: downshear left, DR: downshear right, UL: upshear left, UR: upshear right), following the convention described by DeHart (2014). This quadrant-based decomposition is useful because it provides a consistent framework to interpret storm structure and convective organization under the influence of vertical wind shear. The mentioned classification is based on the direction of the mean environmental vertical wind shear, defined as the difference between the horizontal vector winds at the 850 hPa and 200 hPa pressure levels. The shear is computed within a circular annulus surrounding the storm, delineated by the dotted black curves in Figure 13, which spans from 200 km to 600 km in radius and thus excludes the inner-core region. This environmental shear estimation offers a large-scale characterization of the surrounding wind field and is primarily useful for interpreting the hurricane storm structure and asymmetries (e.g., the inner-core circulation with inflow and outflow features) induced by external forcing.

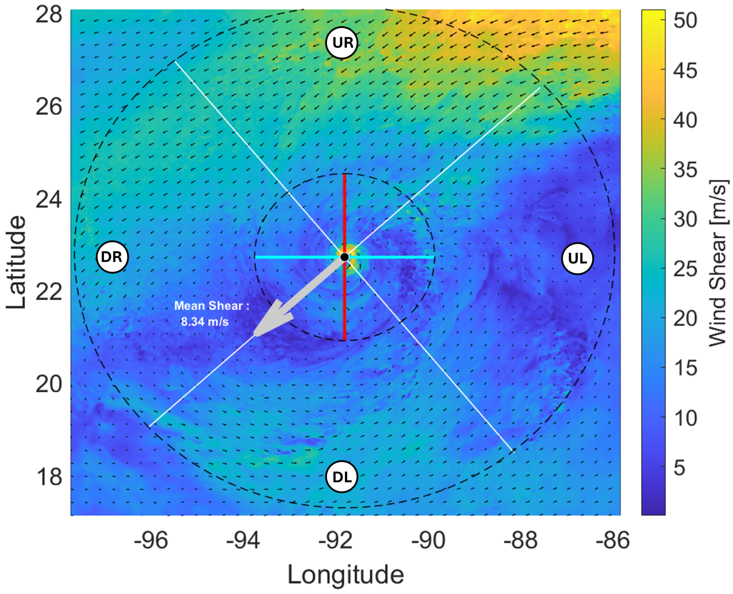

Figure 13. Example of shear-oriented quadrant division for the scene related to Hurricane Milton on 10/07/2024 at 12 UTC. The thin white lines divide the hurricane into four shear-relative quadrants, labeled with their respective acronyms: downshear left (DL), downshear right (DR), upshear left (UL), and upshear right (UR). The gray arrow indicates the direction of the mean large-scale vertical wind shear vector, computed within the annular region between 200 and 600 km from the storm center, as delimited by the black dashed lines. The red and cyan thick lines represent radial cuts that cross the inner-core region of the tropical cyclone (shown in Fig. 14).

Figure 14 presents zonal (cyan line in Fig. 13) and meridional (red line in Fig. 13) vertical cuts through the TC eye. With the previous wind-shear classification, they correspond to four cuts in the middle of the UL, UR, DR and DL domains. In these vertical curtains it is possible to identify the radial inflows and outflows (here each cut is spanning a 400 km wide region). The two profiles display wind speed (left panel) and WIVERN-measured reflectivity (right panel), overlaid with both the modeled wind field (black vectors) and the retrieved wind vectors (red vectors). These radial profiles reveal the asymmetries typically found in tropical cyclones, both in terms of dynamic structure and hydrometeor distribution. Such asymmetries involve complex interactions between horizontal inflows and outflows, as well as convective regions characterized by intense updrafts and downdrafts (see arrows in the right panels of Fig. 14) . These reconstructions clearly demonstrate the potential of WIVERN measurements to shed light on the mechanisms driving the internal circulation of hurricanes, and therefore their organization and possible intensification.

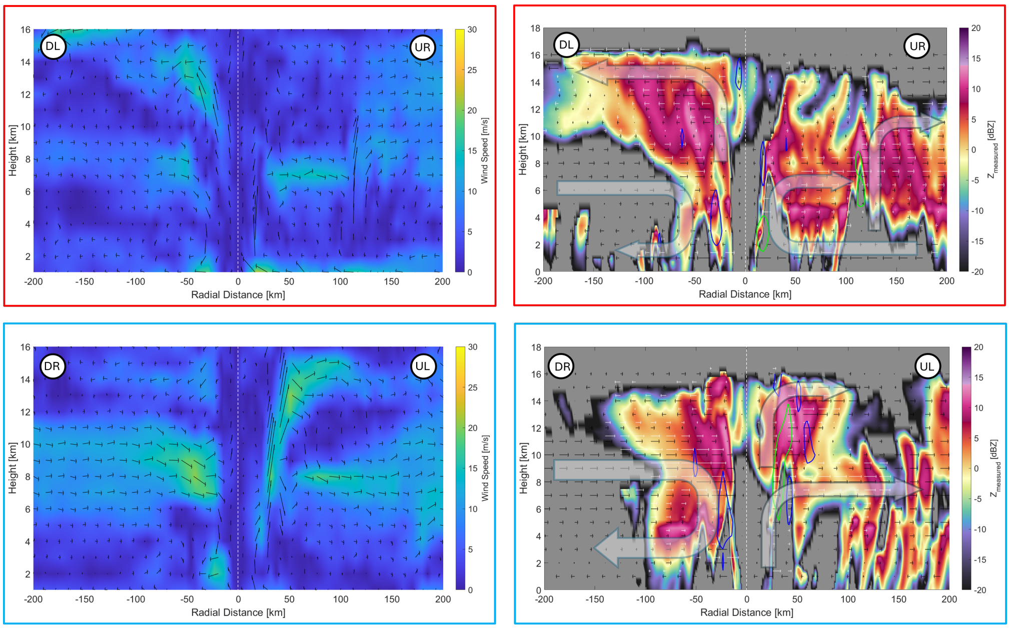

Figure 14. Meridional (top panels) and zonal (bottom panels) vertical cuts across the inner-core region of Hurricane Milton on 10/07/2024 at 12 UTC, each spanning 400 km through the storm center. Left panels show the model wind velocities projected onto the two vertical cuts (arrows) with their corresponding wind speed (color-coded). The right panels display WIVERN-measured reflectivity superimposed with the model horizontally projected radial wind velocities (black arrows) and those retrieved by WIVERN (white arrows) in correspondence to the scanning pattern shown in Fig. 12. Mean circulations within each quadrant are shown by the large arrows. The contour lines highlight convective regions with blue contours corresponding to downdrafts of –1 m/s and green contours indicating updrafts of 3 m/s.

3.2 Tropical Cyclone Intensification

WIVERN will also be able to capture wind features inside the inner core of TCs. While W-band radars are typically limited by signal attenuation in regions with high liquid water content, WIVERN slant view can enable penetration in regions heavily loaded with precipitation (e.g. the eye-wall) from regions that are almost cloud-free (e.g. from the eye). Thanks to the multiple cross-cuts through the hurricane and reduced surface clutter (Coppola et al., 2025), it is possible to retrieve crucial information about the wind in the lower troposphere and inside the eye-wall where the strongest winds occur. The horizontal wind vector swath product described in Sec. 2.4 can represent well the TC large-scale circulation, but its coarse resolution prevents an accurate representation of the dynamics in the presence of very strong wind shear like close to the eye. For the wind structure near the eye a full reconstruction of the wind field can rely on a model; here the very simple one described by cyclostrophic balance as proposed by Holland (1980) is used. The azimuthal symmetric cyclostrophic tangential wind (V_c) can be written as:

$$V_c(r) = V_c(r_{max})\sqrt{\left(\frac{r_{max}}{r}\right)^B e^{\left[1-\left(\frac{r_{max}}{r}\right)^B\right]}} \tag{2}$$

540 where r_{max} is the radius of maximum wind and B is an non-dimensional parameter re-
541 lated to the maximum wind velocity by $V_c(r_{max}) = \sqrt{B\,(p_n - p_c)/(\rho\, e)}$ where ρ is the
542 air density, p_c and p_n are the central and ambient pressure, e is the Neper number.

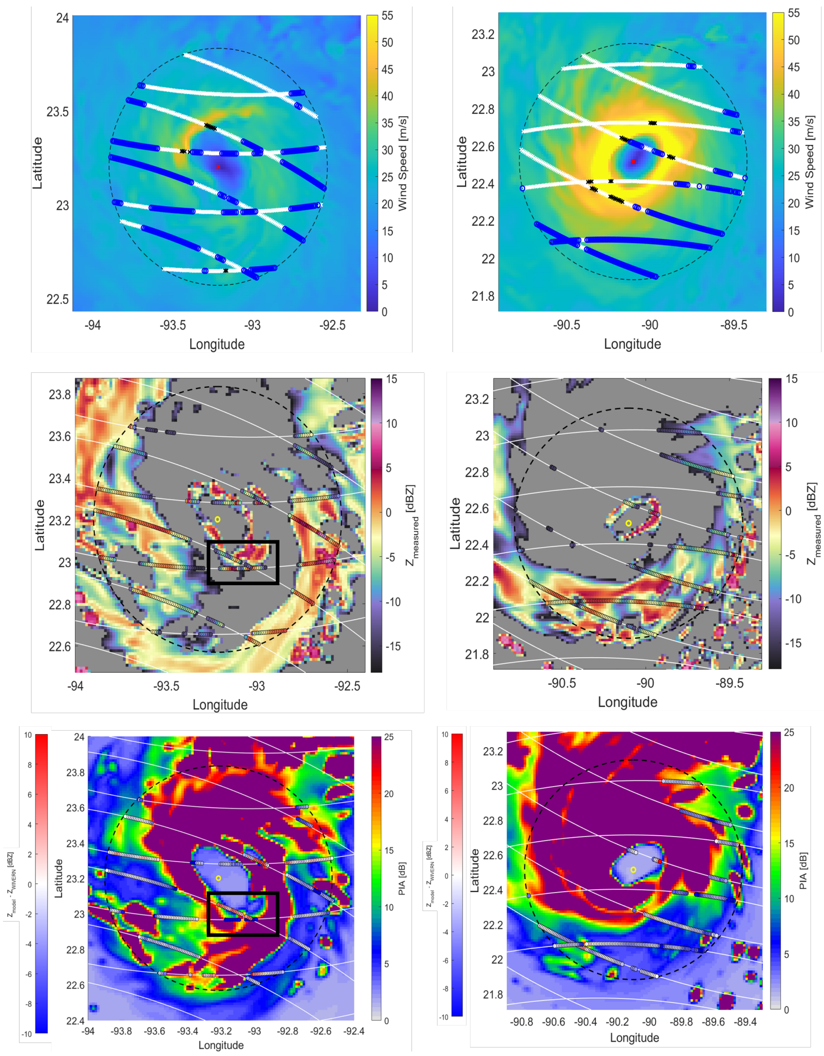

Figure 15. Inner core (i.e. distance from TC eye lower than 70 km as indicated by the black dashed circles) WIVERN sampling of Hurricane Milton at a 2 km altitude, before (left side) and after (right side) the rapid intensification occurred on 8 October 2024. Top panels: the scanning tracks of the antenna boresight are plotted above the two-dimensional hurricane horizontal wind speed field (color coded). WIVERN measurements discharged due to low reflectivity are marked with white crosses, those excluded due to high vertical wind velocity with black crosses, and valid measurements are indicated by blue circles. Middle panels: the model 1D-simulated reflectivity is colorcoded, while circles color-coded with the same color-bar along the WIVERN track represent WIVERN-measured reflectivity values accounting for the full three-dimensional geometry. Lower panels: PIA field of the two scenes with superimposed WIVERN track with colored circles color-coded with the color-bar on the left hand side representing the difference between the two aforementioned reflectivity values. The black rectangle in the left panels shows an interesting portion of track that is further analyzed in Fig. 16.

The WIVERN measurements of the two successive overpasses, one before and one after the rapid intensification that occurred to Milton on 8 Oct 2024 (thick cyan lines labeled as 2 and 3 in Fig. 6), are used to optimally fit the three free parameters of the model of Holland (1980) ($V_c(r_{max})$, r_{max}, B). An appropriate filtering process was applied to the measurements acquired at an altitude of 2 km, as presented in the top two panels of Fig. 15. This included discarding data points where the reflectivity was below -18 dBZ, indicating an insufficient presence of hydrometeors to serve as tracers for wind estimation, or where the vertical velocity exceeded 2 m/s, typically associated with strong convective towers. Additionally, measurements with a Signal-to-Clutter Ratio (SCR) below 20 dB were excluded, as they indicate contamination of the Doppler signal by surface contributions.

In this context, WIVERN ability to measure LoS Doppler velocities from a slant view enables winds in otherwise inaccessible regions to be observed. The slanted geometry plays a key role in determining reflectivity measurements. This feature is well highlighted by the two middle panels of Fig. 15, where the measured reflectivity derived from the hurricane model output (background) is compared to the one produced by the WIVERN simulator (colored circles on WIVERN white scanning track). In first approximation, when attenuated reflectivity is estimated from model data, each atmospheric column is treated independently as a purely vertical one-dimensional profile. The Path-Integrated Attenuation (PIA) is computed by integrating the extinction coefficient vertically, and then subtracted from the unattenuated model reflectivity (accounting for the slant geometry with an amplification factor equal to $1/\cos(\theta_I) \approx 1.34$) to obtain a first approximation attenuated reflectivity. However, this simplification does not take into account the actual path followed by the radar pulse when propagating though the atmosphere. In contrast, the WIVERN simulator accounts for the true three-dimensional propagation of the radar beam along its slant path. It simulates how the signal interacts with the volume of atmosphere it traverses, thus properly capturing attenuation effects. Consequently, differences between the model-derived and simulator-derived attenuated reflectivity fields can be attributed to three-dimensional effects, which will be particularly relevant in regions characterized by large spatial variability of the hydrometeor structures, thus of the PIA field. These are made evident in the lower panel of Fig. 15, where the difference between the two reflectivity estimates is superimposed on the PIA field, enabling the identification of areas where WIVERN slant-view geometry provides a clear advantage by avoiding heavily attenuating regions. A portion of the observation track, highlighted by the black rectangle in the left side panels of Fig. 15, demonstrates this phenomenon. A zoomed-in view of this area is presented in Fig. 16, where it is possible to distinguish two distinct scenarios. In the case of the red-colored circles, the reflectivity derived from the model exceeds that observed by WIVERN. This occurs because, in the layers above 2 km, the actual radar beam crosses the eye-wall where strong attenuation strongly reduces the radar return. In contrast, the blue-colored circles correspond to observations where the radar beam penetrates from the eye, a region with relatively low attenuation. Here, WIVERN will measure reflectivity values that are higher than those expected from the model-1D approximation estimate, highlighting the radar ability to access regions typically inaccessible to conventional nadir-viewing systems. In summary, the WIVERN slant view is not always detrimental because of the increased slant attenuation. In deep convection, it sometimes allows penetrations into regions in the lower troposphere that are inaccessible by a W-band nadir-looking radar.

The WIVERN measurements are used to retrieve the three free parameters of Holland model through a least-squares fitting procedure using data acquired before and after the rapid intensification phase. The cost function minimization enables the selection of the optimal set of three parameters that best reproduce the cyclostrophic wind field within the first 70 km from the TC center. Fig. 17 shows the azimuthal average around the TC eye of the horizontal winds as a function of the radial distance from the eye of the hurricane for the model outputs (circles) and obtained by using a least square best

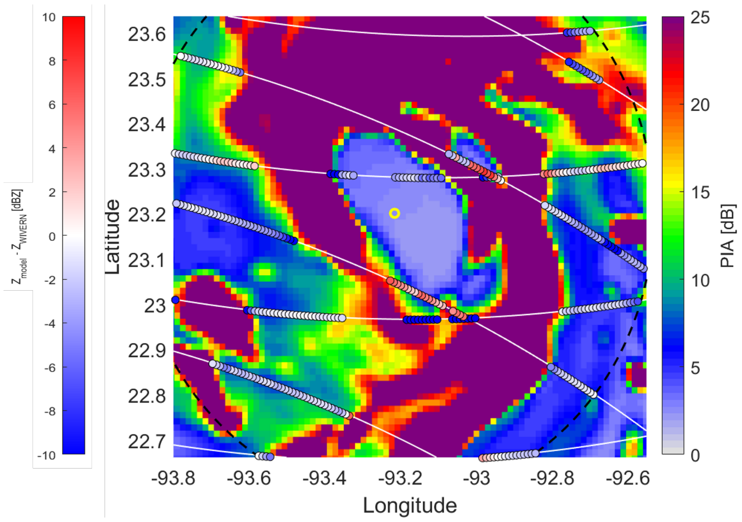

Figure 16. Zoomed-in view of the observation track segment highlighted in Figure 15.

fitting procedure using WIVERN data before and after the rapid intensification. As demonstrated in Fig. 17 WIVERN measurements can properly capture the acceleration of winds from 30 to 60 m/s occurring in less than 24 h. The retrieved parameters of the model proposed by Holland (1980) produce the thick continuous curves that are almost superimposed to the best-fit curves (thin dashed lines) of the azimuthally averaged wind speeds (circles).

This example demonstrates that WIVERN can provide insight in really extreme weather scenarios and that, thanks to its frequent overpasses over TCs, it can actually identify rapid intensification. Note that, in the best situation, two consecutive overpasses within 400 km can occur with one ascending and one descending orbit separated by 12 h or with two ascending or two descending orbits separated by 24 h (like in the previous example, orbits (2) and (3) in Fig. 6).

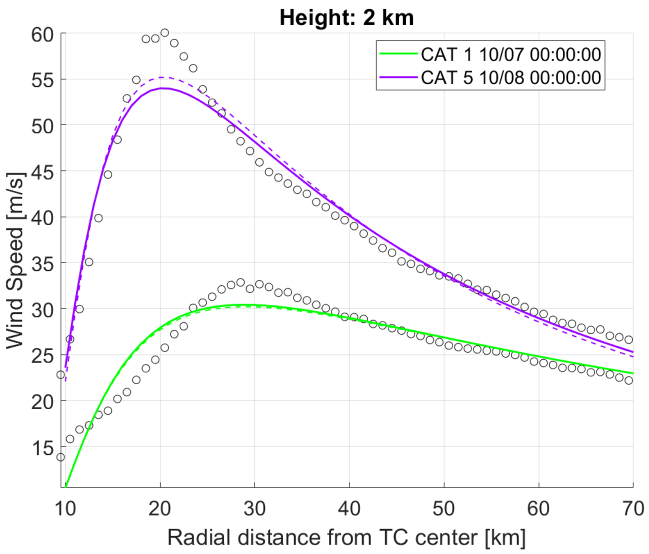

Figure 17. Wind inside hurricane Milton at 2 km height before and after the rapid intensification occurred on the 8 Oct 2024. Two descending orbits separated by 24 h have been used (thick cyan lines in Fig. 6). The true azimuthally averaged winds are plotted with circles with maximum wind speeds of 32 m/s before and 60 m/s after intensification reached at 30 and 20 km from the TC centre, respectively. WIVERN measurements well reproduce the model proposed by Holland (1980).

3.3 Profiling ice mass

The WIVERN IWC retrieved with the methodology discussed in Sect. 2.5 can be cumulated to produce vertical distribution of the ice mass contents as a function of the distance from the TC eye. The results for the overpass shown in Fig. 10 are depicted in Fig. 18 with each annulus having a thickness of 10 km. Overall there is a very good agreement between the model (left) and the WIVERN reconstructed IWC fields (right). Discrepancies (negative biases), caused by the WIVERN sensitivity threshold (5 mg/m^3) are found in correspondence of regions with very low IWCs (right panel).

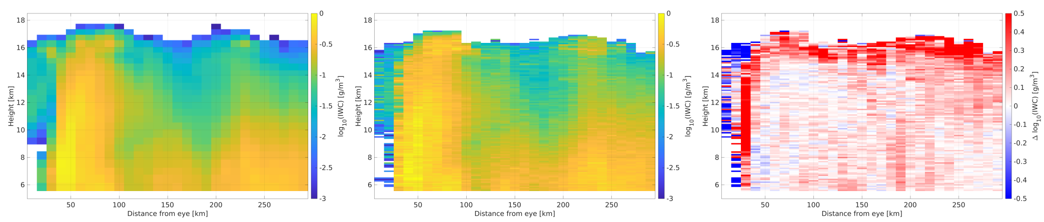

Figure 18. Vertical distribution of the ice mass contents as a function of the distance from the TC eye for the overpass shown in Fig. 10 with the WRF model output (left) and reconstructed from a single WIVERN overpass (centre panel). The right panel shows the difference between WIVERN and the model distribution.

A statistical analysis of the IWC retrieval performance is carried out by running multiple overpassess with different orbits corresponding to 25 different snapshots of hurricane Milton straddling the rapid intensification period between 10 UTC on 6 October and 08 UTC on 7 October. The errors in the retrieved IWC are computed for the 15 different scenes. The standard deviation and the mean of such errors is shown in Fig. 19. Results demonstrate that the WIVERN estimates are generally unbiased (bias generally lower than a factor of 1.25 (left panel in Fig. 19), with some positive bias only at cloud top) with standard deviation lower than a factor of 1.5 (right panel in Fig. 19).

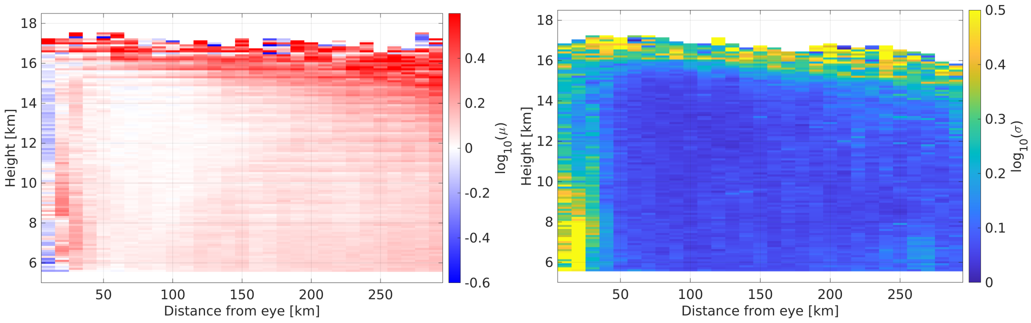

Figure 19. IWC retrieval performances: expected bias (left) and standard deviation (right) as a function of height and of the distance from the eye. Resulst are based on 25 different snapshots for Hurricane Milton from 10 UTC of 06/10 to 8 UTC of 07/10 with WIVERN orbits crossing the hurricane at different distances from the eye center (from 0 to 100 km).

4 Conclusions

The WIVERN concept, one of the remaining two candidates in the ESA Earth Explorer 11 selection program, is set to enhance the TC global observing system in a way that is unparalleled.

Using simulations of Hurricane Milton as a test bed, this study demonstrates that WIVERN conically scanning and Doppler capabilities will enable unprecedented sampling capability of the vertical structure of ice mass and of the horizontal winds across the full extent of TCs. WIVERN data can be interpolated to three-dimensional fields of ice mass and horizontal winds at unrivaled vertical and horizontal resolution.

The simulations of several WIVERN overpasses of Hurricane Milton demonstrate that WIVERN Level-3 three-dimensional horizontal wind vector field products, which are derived directly from the line-of-sight Doppler measurements, effectively reconstruct the three-dimensional horizontal wind structure of the storm. This is particularly evident in glaciated areas, where the products capture vertical wind shear, upper-level divergences and in-cloud circulations. Additionally, successive WIVERN overpasses (with a minimum time interval of 12 hours in the most favorable circumstances) enable observation of storm evolution, specifically wind intensity within the inner core of the lower troposphere, including phases of intensification or weakening.

WIVERN reflectivity measurements also allows the vertical distribution of ice mass to be retrieved. Despite not detecting IWCs smaller than 5 mg/m^3, WIVERN will be able to determine the height and distance from the TC eye at which the ice will be detrained and to quantify its mass.

The synergy between the Level-3 three-dimensional ice mass field product and the Level-3 three-dimensional horizontal wind vector field has the potential to provide crucial insights in TC dynamical and thermodynamic and microphysical structure and to a better understanding of the nexus between water, latent heat and circulation. In particular, it could help to clarify whether the anvil mass originated from the eyewall or the rain bands.

Future work should expand this study to more TC simulations, trying to consolidate the estimates in the the expected errors in the reconstruction of the winds and of the anvil ice mass. More sophisticated techniques for reconstructing the gridded products (e.g. including machine learning methodologies) could be investigated as well.

Acknowledgments

This research has been supported by the European Space Agency under the activities “WInd VElocity Radar Nephoscope (WIVERN) Phase A Science and Requirements Consolidation Study” (ESA Contract Number RFP/3-18420/24/NL/IB/ab). This study was carried out within the Space It Up project funded by the Italian Space Agency (ASI) and the Ministry of University and Research (MUR) under contract no. 2024-5-E.0 – CUP no. I53D24000060005.

This work used the Mafalda and Felipe High Performance Computing Facilities at Politecnico di Torino.

Data Availability Statement

The WRF simulations outputs of Hurricane Milton and the WIVERN simulations with the different geometry of observations are available upon request to the corresponding author.

References

Avenas, A., Mouche, A., Tandeo, P., Piolle, J.-F., Chavas, D., Fablet, R., … Chapron, B. (2023). Reexamining the estimation of tropical cyclone radius of maximum wind from outer size with an extensive synthetic aperture radar dataset. *Monthly Weather Review*, *151*(12), 3169 - 3189. Retrieved from https://journals.ametsoc.org/view/journals/mwre/151/12/MWR-D-23-0119.1.xml doi: 10.1175/MWR-D-23-0119.1

Battaglia, A., Cambiotti, C., Carbone, A. F., & Da Silva, S. (2024). Reconstruction of the horizontal wind field inside weather systems from the sparse sampling envisaged for the wind velocity radar nephoscope (wivern) mission. In *Igarss 2024 - 2024 ieee international geoscience and remote sensing symposium* (p. 8925-8927). doi: 10.1109/IGARSS53475.2024.10640420

Battaglia, A., Kollias, P., Dhillon, R., Roy, R., Tanelli, S., Lamer, K., … Furukawa, K. (2020a). Spaceborne cloud and precipitation radars: Status, challenges, and ways forward. *Reviews of Geophysics*, *58*(3), e2019RG000686. Retrieved from https://agupubs.onlinelibrary.wiley.com/doi/abs/10.1029/2019RG000686 (e2019RG000686 10.1029/2019RG000686) doi: 10.1029/2019RG000686

Battaglia, A., Kollias, P., Dhillon, R., Roy, R., Tanelli, S., Lamer, K., … Furukawa, K. (2020b). Spaceborne cloud and precipitation radars: Status, challenges, and ways forward. *Reviews of Geophysics*, *58*(3), e2019RG000686. Retrieved from https://agupubs.onlinelibrary.wiley.com/doi/abs/10.1029/2019RG000686 (e2019RG000686 10.1029/2019RG000686) doi: 10.1029/2019RG000686

Battaglia, A., Martire, P., Caubet, E., Phalippou, L., Stesina, F., Kollias, P., & Illingworth, A. (2022). Observation error analysis for the wind velocity radar nephoscope w-band doppler conically scanning spaceborne radar via end-to-end simulations. *Atmospheric Measurement Techniques*, *15*(9). doi: 10.5194/amt-15-3011-2022

Battaglia, A., Rabino, R., Mroz, K., Tridon, F., & Parodi, A. (2025). Non uniform beam filling correction for the doppler velocity measured by the wivern conically scanning radar. *J. Atmos. Ocean Technol.*. (submitted)

Battaglia, A., Rizik, A., Sikaneta, I., & Tridon, F. (2025). I and qs simulation and processing envisaged for spaceborne polarization diversity doppler radars. *IEEE Trans. Geosci. Remote Sens.*, *63*, 1-14. doi: 10.1109/TGRS.2025.3529672

Benjamin, S. G., Grell, G. A., Brown, J. M., Smirnova, T. G., & Bleck, R. (2004). Mesoscale weather prediction with the ruc hybrid isentropic–terrain-following coordinate model. *Monthly Weather Review*, *132*(2), 473–494.

Coppola, M., Battaglia, A., Tridon, F., & Kollias, P. (2025). How close to the surface could a spaceborne conically scanning W-band Doppler radar see? *Atm. Meas. Tech. Disc.*. (submitted)

Da Silva, S., Battaglia, A., Cambiotti, C., & Carbone, A. F. (2025). Sparse sampling reconstruction of wind fields for space-borne doppler radars. *IEEE Trans. Geosci. Remote Sens.*. (submitted) doi: XXXXX

DeHart, R., Houze. (2014). Quadrant distribution of tropical cyclone inner-core kinematics in relation to environmental shear. *American Meteorological Society*, 2713–2732. doi: https://doi.org/10.1175/JAS-D-13-0298.1

Emanuel, K. (2001). Contribution of tropical cyclones to meridional heat transport by the oceans. *Journal of Geophysical Research: Atmospheres*, *106*(D14), 14771-14781. doi: https://doi.org/10.1029/2000JD900641

Emanuel, K. (2003). Tropical cyclones. *Annual Review of Earth and Planetary Sciences*, *31*(1), 75-104. doi: 10.1146/annurev.earth.31.100901.141259

Emanuel, K., DesAutels, C., Holloway, C., & Korty, R. (2004). Environmental control of tropical cyclone intensity. *J. Atmos. Sci.*, *61*(7), 843 - 858. Retrieved from `https://journals.ametsoc.org/view/journals/atsc/61/7/1520-0469_2004_061_0843_ecotci_2.0.co_2.xml` doi: 10.1175/1520-0469(2004)061⟨0843:ECOTCI⟩2.0.CO;2

ESA WIVERN Team. (2025). *Report for mission selection: Earth explorer 11 candidate mission wivern* (Tech. Rep.). ESA-EOPSM-WIVE-RP-4798. (DOI: 10.5281/zenodo.15607041)

Fiori, E., Ferraris, L., Molini, L., Siccardi, F., Kranzlmueller, D., & Parodi, A. (2017). Triggering and evolution of a deep convective system in the mediterranean sea: Modelling and observations at a very fine scale. *Quarterly Journal of the Royal Meteorological Society*, *143*(703), 927–941.

Fiori, E., Parodi, A., & Siccardi, F. (2010). Turbulence closure parameterization and grid spacing effects in simulated supercell storms. *Journal of the Atmospheric Sciences*, *67*(12), 3870–3890.

Fiori, E., Parodi, A., & Siccardi, F. (2011). Uncertainty in prediction of deep moist convective processes: Turbulence parameterizations, microphysics and grid-scale effects. *Atmospheric research*, *100*(4), 447–456.

Frank, & Ritchie. (2001). Effects of vertical wind shear on the intensity and structure of numerically simulated hurricanes. *American Meteorological Society*, 2249–2269. doi: https://doi.org/10.1175/1520-0493(2001)129⟨2249:EOVWSO⟩2.0.CO;2

Gill, D., Michalakes, J., Dudhia, J., Skamarock, W., & Gopalakrishnan, S. (2004). Nesting in wrf 2.0. In *Wrf/mm5 joint workshop* (pp. 22–25).

Gray, W. M. (1968). Global view of the origin of the tropical disturbances and storms. *Monthly Weather Review*, *96*(10), 669 - 700. Retrieved from `https://journals.ametsoc.org/view/journals/mwre/96/10/1520-0493_1968_096_0669_gvotoo_2_0_co_2.xml` doi: 10.1175/1520-0493(1968)096⟨0669:GVOTOO⟩2.0.CO;2

Hasan, M. B., Guimond, S. R., Yu, M., Reddy, S., & Giraldo, F. X. (2022). The effects of numerical dissipation on hurricane rapid intensification with observational heating. *Journal of Advances in Modeling Earth Systems*, *14*(8), e2021MS002897.

Hendricks, E. A., Peng, M. S., Fu, B., & Li, T. (2010). Quantifying environmental control on tropical cyclone intensity change. *Monthly Weather Review*, *138*(8), 3243 - 3271. Retrieved from `https://journals.ametsoc.org/view/journals/mwre/138/8/2010mwr3185.1.xml` doi: 10.1175/2010MWR3185.1

Hersbach, H., Bell, B., Berrisford, P., Hirahara, S., Horányi, A., Muñoz-Sabater, J., … others (2020). The era5 global reanalysis. *Quarterly journal of the royal meteorological society*, *146*(730), 1999–2049.

Holbach, H. M., Bousquet, O., Bucci, L., Chang, P., Cione, J., Ditchek, S., … Zhang, J. A. (2023). Recent advancements in aircraft and in situ observations of tropical cyclones. *Tropical Cyclone Research and Review*, *12*(2), 81-99. Retrieved from `https://www.sciencedirect.com/science/article/pii/S222560322300022X` doi: https://doi.org/10.1016/j.tcrr.2023.06.001

Holland, G. J. (1980). An analytic model of the wind and pressure profiles in hurricanes. *Monthly Weather Review*, *108*(8), 1212 - 1218. Retrieved from `https://journals.ametsoc.org/view/journals/mwre/108/8/1520-0493_1980_108_1212_aamotw_2_0_co_2.xml` doi: 10.1175/1520-0493(1980)108⟨1212:AAMOTW⟩2.0.CO;2

Hong, S.-Y., Noh, Y., & Dudhia, J. (2006). A new vertical diffusion package with an explicit treatment of entrainment processes. *Monthly weather review*, *134*(9), 2318–2341.

Houze, R. A. (2010). Clouds in tropical cyclones. *Monthly Weather Review*, *138*(2), 293 - 344. Retrieved from `https://journals.ametsoc.org/view/journals/mwre/138/2/2009mwr2989.1.xml` doi: 10.1175/2009MWR2989.1

Iacono, M. J., Delamere, J. S., Mlawer, E. J., Shephard, M. W., Clough, S. A., & Collins, W. D. (2008). Radiative forcing by long-lived greenhouse gases: Calculations with the aer radiative transfer models. *Journal of Geophysical Research: Atmospheres*, *113*(D13).

Illingworth, A. J., Battaglia, A., Bradford, J., Forsythe, M., Joe, P., Kollias, P., … Wolde, M. (2018). WIVERN: A New Satellite Concept to Provide Global In-Cloud Winds, Precipitation, and Cloud Properties. *Bull. Amer. Met. Soc.*, *99*(8), 1669-1687. Retrieved from `https://doi.org/10.1175/BAMS-D-16-0047.1` doi: 10.1175/BAMS-D-16-0047.1

Judt, F., & Chen, S. S. (2016). Predictability and dynamics of tropical cyclone rapid intensification deduced from high-resolution stochastic ensembles. *Monthly Weather Review*, *144*, 4395–4420.

Kalesse, H., & Kollias, P. (2013). Climatology of High Cloud Dynamics Using Profiling ARM Doppler Radar Observations. *J. Climate*, *26*, 6340-6359. (doi: http://dx.doi.org/10.1175/JCLI-D-12-00695.1)

Klotzbach, P. J., Bowen, S. G., Pielke, R., & Bell, M. (2018). Continental u.s. hurricane landfall frequency and associated damage: Observations and future risks. *Bull. Amer. Met. Soc.*, *99*(7), 1359 - 1376. Retrieved from `https://journals.ametsoc.org/view/journals/bams/99/7/bams-d-17-0184.1.xml` doi: https://doi.org/10.1175/BAMS-D-17-0184.1

Knapp, K. R., Kruk, M. C., Levinson, D. H., Diamond, H. J., & Neumann, C. J. (2010). The international best track archive for climate stewardship (ibtracs): Unifying tropical cyclone data. *Bulletin of the American Meteorological Society*, *91*(3), 363 - 376. Retrieved from `https://journals.ametsoc.org/view/journals/bams/91/3/2009bams2755_1.xml` doi: 10.1175/2009BAMS2755.1

Liu, Y., Guan, S., Lin, I.-I., Zhao, W., Jin, F.-F., Liu, P., & Tian, J. (2025). Storm size modulates tropical cyclone intensification through an oceanic pathway in global oceans. *Journal of Climate*, *38*(4), 891 - 908. Retrieved from `https://journals.ametsoc.org/view/journals/clim/38/4/JCLI-D-24-0398.1.xml` doi: 10.1175/JCLI-D-24-0398.1

Manconi, F., Battaglia, A., & Kollias, P. (2025). Characterization of surface clutter signal in the presence of orography for a spaceborne conically scanning w-band doppler radar. *Atmospheric Measurement Techniques*, *18*(10), 2295–2310. Retrieved from https://amt.copernicus.org/articles/18/2295/2025/ doi: 10.5194/amt-18-2295-2025

Marchand, R., Mace, G. G., Ackerman, T., & Stephens, G. (2008). Hydrometeor Detection Using Cloudsat—An Earth-Orbiting 94-GHz Cloud Radar. *J. Atmos. Ocean Technol.*, *25*(4), 519-533. Retrieved from https://doi.org/10.1175/2007JTECHA1006.1 doi: 10.1175/2007JTECHA1006.1

Mouche, A., Chapron, B., Knaff, J., Zhao, Y., Zhang, B., & Combot, C. (2019). Copolarized and cross-polarized sar measurements for high-resolution description of major hurricane wind structures: Application to irma category 5 hurricane. *Journal of Geophysical Research: Oceans*, *124*(6), 3905-3922. Retrieved from https://agupubs.onlinelibrary.wiley.com/doi/abs/10.1029/2019JC015056 doi: https://doi.org/10.1029/2019JC015056

Mustich, F., Battaglia, A., Manconi, F., Kollias, P., & Parodi, A. (2025). CONvective–STRAtiform Identification Neural Network for the WIVERN mission. *Remote Sensing*. (submitted June 2025, available at https://wivern.polito.it/publications/)

Nolan, D. S., Fischer, M. S., & O'Neill, M. E. (2025). Reconsideration of the mass and condensate sources for the tropical cyclone outflow. *Bulletin of the American Meteorological Society*, BAMS-D-24-0284.1. Retrieved from https://journals.ametsoc.org/view/journals/bams/aop/BAMS-D-24-0284.1/BAMS-D-24-0284.1.xml doi: 10.1175/BAMS-D-24-0284.1

Powers, J. G., Klemp, J. B., Skamarock, W. C., Davis, C. A., Dudhia, J., Gill, D. O., ... others (2017). The weather research and forecasting model: Overview, system efforts, and future directions. *Bulletin of the American Meteorological Society*, *98*(8), 1717–1737.

Protat, A., Delanoë, J., Bouniol, D., Heymsfield, A. J., Bansemer, A., & Brown, P. (2007). Evaluation of ice water content retrievals from cloud radar reflectivity and temperature using a large airborne in situ microphysical database. *Journal of Applied Meteorology and Climatology*, *46*(5), 557 - 572. Retrieved from https://journals.ametsoc.org/view/journals/apme/46/5/jam2488.1.xml doi: 10.1175/JAM2488.1

Ricciardulli, L., Howell, B., Jackson, C. R., Hawkins, J., Courtney, J., Stoffelen, A., ... Glaiza Escullar, M. A. (2023). Remote sensing and analysis of tropical cyclones: Current and emerging satellite sensors. *Tropical Cyclone Research and Review*, *12*(4), 267-293. Retrieved from https://www.sciencedirect.com/science/article/pii/S2225603223000553 doi: https://doi.org/10.1016/j.tcrr.2023.12.003

Rios-Berrios, R., Finocchio, P. M., Alland, J. J., Chen, X., Fischer, M. S., Stevenson, S. N., & Tao, D. (2024). A review of the interactions between tropical cyclones and environmental vertical wind shear. *Journal of the Atmospheric Sciences*, *81*(4), 713 - 741. Retrieved from https://journals.ametsoc.org/view/journals/atsc/81/4/JAS-D-23-0022.1.xml doi: 10.1175/JAS-D-23-0022.1

Rizik, A., Battaglia, A., Tridon, F., Scarsi, F. E., Kötsche, A., Kalesse-Los, H., ... Illingworth, A. (2023). Impact of crosstalk on reflectivity and doppler measurements for the wivern polarization diversity doppler radar. *IEEE Transactions on Geoscience and Remote Sensing*, *61*, 1-14. doi: 10.1109/TGRS.2023.3320287

Rogers, R., Reasor, P., & Lorsolo, S. (2013). Airborne doppler observations of the inner-core structural differences between intensifying and steady-state tropical cyclones. *Monthly Weather Review*, *141*(9), 2970 - 2991. Retrieved from https://journals.ametsoc.org/view/journals/mwre/141/9/mwr-d-12-00357.1.xml doi: 10.1175/MWR-D-12-00357.1

Scarsi, F. E., Battaglia, A., Maahn, M., & Lhermitte, S. (2024). How to reduce sampling errors in spaceborne cloud radar-based snowfall estimates. *EGUsphere*, *2024*, 1–23. Retrieved from https://egusphere.copernicus.org/preprints/2024/egusphere-2024-1917/ doi: 10.5194/egusphere-2024-1917

Schenkel, B. A., Edwards, R., & Coniglio, M. (2020). A climatological analysis of ambient deep-tropospheric vertical wind shear impacts upon tornadoes in tropical cyclones. *Weather and Forecasting*, *35*(5), 2033 - 2059. Retrieved from https://journals.ametsoc.org/view/journals/wefo/35/5/wafD190220.xml doi: https://doi.org/10.1175/WAF-D-19-0220.1

Scoccimarro, E., Gualdi, S., Bellucci, A., Sanna, A., Fogli, P. G., Manzini, E., … Navarra, A. (2011). Effects of tropical cyclones on ocean heat transport in a high-resolution coupled general circulation model. *Journal of Climate*, *24*(16), 4368 - 4384. Retrieved from https://journals.ametsoc.org/view/journals/clim/24/16/2011jcli4104.1.xml doi: https://doi.org/10.1175/2011JCLI4104.1

Skamarock, W. C., Klemp, J. B., Dudhia, J., Gill, D. O., Liu, Z., Berner, J., … others (2019). A description of the advanced research wrf model version 4. *National Center for Atmospheric Research: Boulder, CO, USA*, *145*(145), 550.

Smirnova, T. G., Brown, J. M., & Benjamin, S. G. (1997). Performance of different soil model configurations in simulating ground surface temperature and surface fluxes. *Monthly Weather Review*, *125*(8), 1870–1884.

Smirnova, T. G., Brown, J. M., Benjamin, S. G., & Kim, D. (2000). Parameterization of cold-season processes in the maps land-surface scheme. *Journal of Geophysical Research: Atmospheres*, *105*(D3), 4077–4086.

Soci, C., Hersbach, H., Simmons, A., Poli, P., Bell, B., Berrisford, P., … others (2024). The era5 global reanalysis from 1940 to 2022. *Quarterly Journal of the Royal Meteorological Society*, *150*(764), 4014–4048.

Thatcher, L., & Pu, Z. (2011). How vertical wind shear affects tropical cyclone intensity change: An overview. In A. Lupo (Ed.), *Recent hurricane research* (chap. 13). Rijeka: IntechOpen. Retrieved from https://doi.org/10.5772/15416 doi: 10.5772/15416

Thompson, G., & Eidhammer, T. (2014). A study of aerosol impacts on clouds and precipitation development in a large winter cyclone. *Journal of the atmospheric sciences*, *71*(10), 3636–3658.

Tourville, N., Stephens, G., DeMaria, M., & Vane, D. (2015). Remote sensing of tropical cyclones: Observations from cloudsat and a-train profilers. *Bull. Amer. Met. Soc.*, *96*(4), 609 - 622. Retrieved from https://journals.ametsoc.org/view/journals/bams/96/4/bams-d-13-00282.1.xml doi: 10.1175/BAMS-D-13-00282.1

Tridon, F., Battaglia, A., Rizik, A., Scarsi, F. E., & Illingworth, A. (2023). Filling the gap of wind observations inside tropical cyclones. *Earth and Space Science*, *10*(11), e2023EA003099. Retrieved from https://agupubs.onlinelibrary.wiley.com/doi/abs/10.1029/2023EA003099 (e2023EA003099 2023EA003099) doi: https://doi.org/10.1029/2023EA003099

Wadler, J. B., Cione, J. J., Zhang, J. A., Kalina, E. A., & Kaplan, J. (2022). The effects of environmental wind shear direction on tropical cyclone boundary layer thermodynamics and intensity change from multiple observational datasets. *Monthly Weather Review*, *150*(1), 115 - 134. Retrieved from https://journals.ametsoc.org/view/journals/mwre/150/1/MWR-D-21-0022.1.xml doi: https://doi.org/10.1175/MWR-D-21-0022.1

Wang, H., Zhao, D., Xu, H., Wang, Q., Liang, J., & Yen, T.-H. (2025). The role of wishe in the rapid intensification of super typhoon hinnamnor (2022). *Journal of Geophysical Research: Atmospheres*, *130*(1), e2024JD041864. Retrieved from https://agupubs.onlinelibrary.wiley.com/doi/abs/10.1029/2024JD041864 (e2024JD041864 2024JD041864) doi: https://doi.org/10.1029/2024JD041864

Wu, C.-C., Wu, S.-N., Wei, H.-H., & Abarca, S. F. (2016). The role of convective heating in tropical cyclone eyewall ring evolution. *Journal of the Atmospheric Sciences*, *73*(1), 319 - 330. Retrieved from `https://journals.ametsoc.org/view/journals/atsc/73/1/jas-d-15-0085.1.xml` doi: 10.1175/JAS-D-15-0085.1

Wu, S.-N., & Soden, B. J. (2017). Signatures of tropical cyclone intensification in satellite measurements of ice and liquid water content. *Monthly Weather Review*, *145*(10), 4081 - 4091. Retrieved from `https://journals.ametsoc.org/view/journals/mwre/145/10/mwr-d-17-0046.1.xml` doi: 10.1175/MWR-D-17-0046.1

Yurovskaya, M., Kudryavtsev, V., & Chapron, B. (2023). A self-similar description of the wave fields generated by tropical cyclones. *Ocean Modelling*, *183*, 102184. Retrieved from `https://www.sciencedirect.com/science/article/pii/S1463500323000252` doi: https://doi.org/10.1016/j.ocemod.2023.102184

Zehr, R., et al. (1976). *Tropical disturbance intensification* (No. 259). Department of Atmospheric Science, Colorado State University.